



Dynamical Properties for a Tunable Circular to Polygonal Billiard

Diogo Ricardo da Costa^{1,2}  · André Fujita² · Matheus Rolim Sales³ · José D. Szezech Jr⁴ · Antonio Marcos Batista⁴

Received: 16 November 2021 / Accepted: 14 February 2022 / Published online: 12 March 2022

© The Author(s) under exclusive licence to Sociedade Brasileira de Física 2022

Abstract

In this paper, we introduce a billiard whose boundary varies from a circular to a polygonal billiard. To describe the billiard boundary, we use a parametric equation, which needs to be solved numerically. We provide a detailed explanation about how to obtain the radius of the billiard boundary R for each angular position θ , where we used a tangent method to speed up the numerical simulations. We consider another tangent method to find the billiard boundary's intercept and the particle's trajectory. Furthermore, we show some trajectories' examples and describe what happens with the phase space and Lyapunov exponents when changing the deformation. We present results for different values of the control parameter related to the number of edges of our polygon and the billiard with a triangular-like boundary.

Keywords Nonlinear dynamics · Chaos · Billiard systems · Chaotic system

1 Introduction

According to the literature, a billiard is a closed domain in which classical particles suffer specular collisions with the boundaries. Depending on the billiard boundary's shape, we can find regular, mixed, or fully chaotic dynamics [1–3].

André Fujita and Matheus Rolim Sales both are equally contributed.

 Diogo Ricardo da Costa
diogocost2@gmail.com

André Fujita
andrefujita@usp.br

Matheus Rolim Sales
matheusrolim95@gmail.com

José D. Szezech Jr
jdsjunior@uepg.br

Antonio Marcos Batista
antoniomarcosbatista@gmail.com

¹ Department of Physics, Federal University of Paraná (UFPR), Curitiba 80060-000, PR, Brazil

² Institute of Mathematics and Statistics, University of São Paulo (USP), Rua do Matão, 1010, São Paulo 05508-090, SP, Brazil

³ Graduate Program in Physics, State University of Ponta Grossa, Ponta Grossa 84030-900, PR, Brazil

⁴ Department of Mathematics and Statistics, State University of Ponta Grossa, Ponta Grossa 84030-900, PR, Brazil

There are many different applications for both classical and quantum cases [1, 4]. Some applications to physical problems include the study of ultra-cold atoms trapped in a laser potential [5–8], superconducting and confinement of electrons in semiconductors by electric potentials [4, 9, 10], a reflection of light from mirrors [11], waveguides [12–16], mesoscopic quantum dots [17], and billiard wave functions [18].

In this paper, we consider the dynamics of classical particles confined inside a billiard system whose boundary is changing smoothly from a circular to a polygonal shape. It is a generalization of the triangular-like billiard shown in Ref. [1], where it shows an application for the quantum case. Furthermore, the boundaries' variation plays a vital role in the emergence of a chaotic sea and its extension.

We organized the paper as follows: In Sect. 2, we show how to find the billiard boundary R , where a tangent method finds the correct solution for each angle θ . After that, we apply another tangent method to find the subsequent collisions. These collisions occur when the particle's trajectory intercepts the billiard boundary. It is a challenging task because it is necessary to solve a transcendental equation. Section 3 presents our numerical findings, where we show examples for different polygons and calculate the corresponding Lyapunov exponents. Our final remarks are in Sect. 4, while the acknowledgements section presents our acknowledgments.

2 Model and Methods

Let θ be the angular position, ϵ be a control parameter that changes the boundary shape and permits the recovery of a circular billiard for $\epsilon = 0$, and γ is an integer. Then, we define the tunable circular to polygonal billiard as the following parametric equation:

$$R^2 + \frac{2\sqrt{3}\epsilon}{9} \frac{R^3}{R_0} \cos(\gamma\theta) = R_0^2, \quad \theta \in [0, 2\pi]. \quad (1)$$

Notice that for $\gamma = 3$ and $\gamma = 4$, we recover triangular [1] and square-like billiards [19].

In our simulations, we consider $R_0 = 1$ and

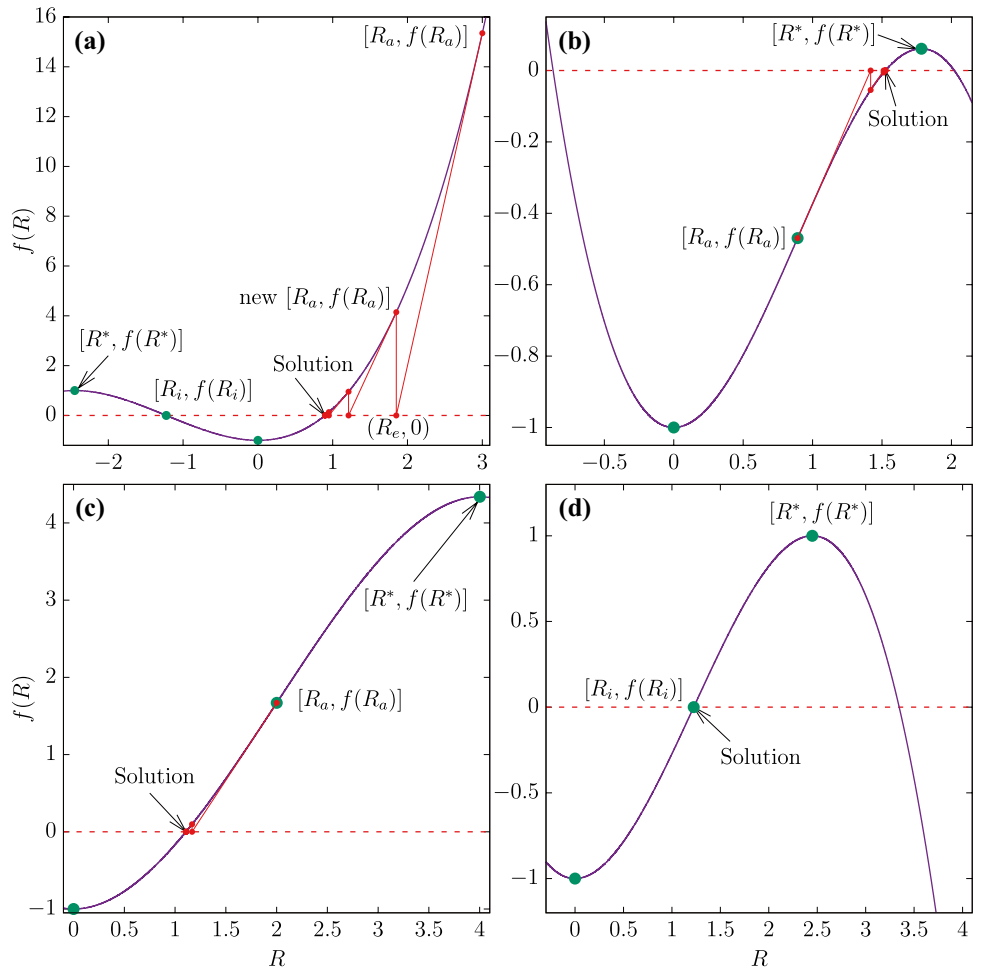
$$a = \frac{2\sqrt{3}\epsilon}{9} \cos(\gamma\theta). \quad (2)$$

Then, we obtain the following equation:

$$f(R) = R(\theta)^2 + aR(\theta)^3 - 1 = 0, \quad \theta \in [0, 2\pi]. \quad (3)$$

Our first task is to find the solutions of $R(\theta)$.

Fig. 1 A plot of $f(R)$ vs R for different situations: In panel (a), we present $R^* < 0$, while in panels (b), (c), and (d), we have three examples of $R^* > 0$



2.1 A Method to Find $R(\theta)$

There is a method to solve cubic equations, known as the Cardano-Tartaglia method. The method consists in rewriting Eq. (3) as follows

$$\left(\frac{1}{a}\right)R^2 + R^3 - \left(\frac{1}{a}\right) = 0, \quad \theta \in [0, 2\pi]. \quad (4)$$

However, the problem with this equation arises when $a \rightarrow 0$, leading to $\frac{1}{a} \rightarrow \infty$. According to Eq. (2), it happens for

$$\cos(\gamma\theta) \rightarrow 0. \quad (5)$$

To avoid numerical errors, it is convenient to consider a numerical method to obtain the solutions.

We start by calculating the local maximum and minimum values of the function $f(R)$ given by Eq. (3). To do that, we need to solve

$$f'(R) = \frac{\partial f}{\partial R} = 0 \Rightarrow R(3aR + 2) = 0. \quad (6)$$

Therefore, the solutions are $R = R^* = -\frac{2}{3a}$ or $R = R^{**} = 0$. The second derivative of f is $f''(R) = \partial^2 f / \partial R^2 = 6aR + 2$. By substituting the solutions R^* and R^{**} , it is possible to show that these solutions correspond to a maximum and minimum function f , respectively. Figure 1 displays four different sketches of f vs R . First, we show an example of a situation in which $R^* < 0$ (Fig. 1(a)), while in Fig. 1(b), (c), and (d), we have three examples of $R^* > 0$.

By solving $\frac{\partial^2 f(R)}{\partial R^2} = 0$, it is possible to find the inflection point of $f(R)$, named R_i . It leads us to the following solution

$$R_i = -\frac{1}{3a} = \frac{R^*}{2}. \quad (7)$$

It is also possible to obtain the value of $f(R_i)$, as follows

$$f(R_i) = \frac{4}{27a^2} - 1, \quad (8)$$

which is similar to $f(R^*)$,

$$f(R^*) = \frac{2}{27a^2} - 1. \quad (9)$$

Figure 2(a), (b), (c), and (d) exhibit the position of the inflection point $[R_i, f(R_i)]$ and the position of the local maximum $[R^*, f(R^*)]$ for different values of θ . For instance, when $\theta = -\frac{\pi}{2\gamma}$ or $\theta = +\frac{\pi}{2\gamma}$, we see that $R_i = R^* \rightarrow \pm\infty$ and $f(R_i) = f(R^*) \rightarrow \infty$. It happens when $a \rightarrow 0$, leading to $\cos(\gamma\theta) \rightarrow 0$. The angle θ that makes $R_i = R^* \rightarrow \pm\infty$ is

$$[\theta]_{R_i \rightarrow \pm\infty} = \frac{\pi(2z - 1)}{2\gamma}, \quad (10)$$

Fig. 2 In panels (a) and (b), we have the inflection point $[R_i, f(R_i)]$ as a function of θ . In panels (c) and (d), the position of the local maximum $[R^*, f(R^*)]$. An inflection point is a point on the graph of the function $f(R)$ in which the concavity changes

where $z \in \mathbb{Z}$. This value is independent of the ϵ value chosen.

We obtain the local maximums and minimums of the curves R^* and R_i , when $\cos(\gamma\theta) = +1$. After solving this equation, we find the angle θ that turns R^* and R_i as local maximums named $[\theta]_{R_{\max}^*}$, equal to

$$[\theta]_{R_{\max}^*} = \frac{2\pi k}{\gamma}, \quad (11)$$

where $K \in \mathbb{Z}$ and the curvature are negative. It occurs, for example, when $\theta = 0$ (or $K = 0$) in Fig. 2(a) and (c).

Figure 2(a) and (c) show that R_i is also a local minimum exactly at the same position of the curve R^* . To calculate the local minimum of both R_i and R^* , we consider $\cos(\gamma\theta) = -1$, which happens when θ is

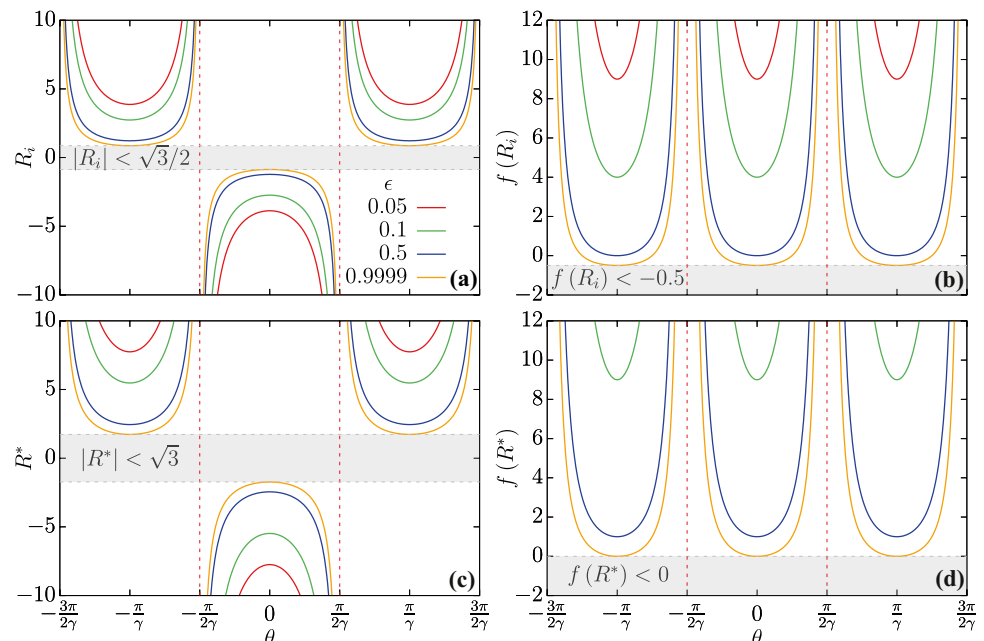
$$[\theta]_{R_{\min}^*} = \frac{2\pi k + \pi}{\gamma}, \quad (12)$$

where again $k \in \mathbb{Z}$. These local minimums emerge, for example, when $\theta = -\frac{\pi}{\gamma}$ and $\theta = +\frac{\pi}{\gamma}$ in Fig. 2(a) and (c).

Figure 2(a), (b), (c), and (d) exhibit gray regions where the curves of R_i , R^* , $f(R_i)$, and $f(R^*)$ cannot reach. When $\epsilon \rightarrow 1$, these curves approach the gray region.

2.2 Tangent Method

To calculate the solution of $f(R) = 0$, we use a tangent method. According to Fig. 1(a), we call R_a the initial approximation, with $f(R_a)$ being the value of f . In our simulations,



$R_a = 3$ if $|a| < 10^{10}$ (which avoids division by zero), $R^* < 0$ or $R_i > 3$, otherwise $R_a = R_i$.

A tangent line that passes through $(R_a, f(R_a))$ is

$$f = f(R_a) + R_a(3aR_a + 2)(R - R_a). \quad (13)$$

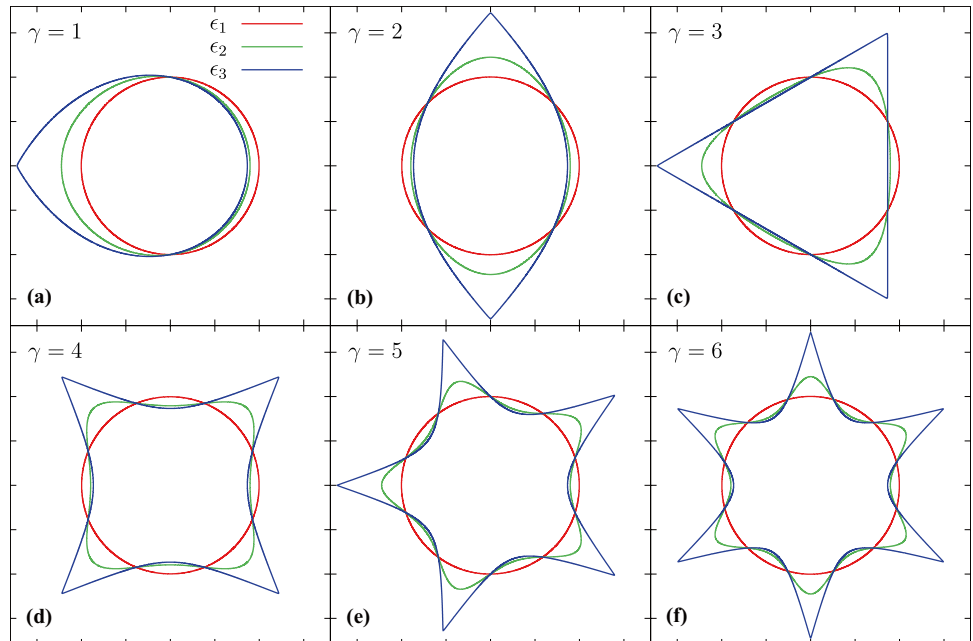
Our tangent method's fundamental idea is to obtain the tangent line intercept with the horizontal line $f(R) = 0$. We represent it by the red dashed line in Fig. 1(a). We can accomplish this by considering $f = 0$ in Eq. (13), which leads us to the following solution

$$R_e = R_a - \frac{f(R_a)}{R_a(3aR_a + 2)}, \quad (14)$$

where $(R_e, 0)$ is the intercept position. Now, we consider a recursive method. We obtain the new position $[R_a, f(R_a)]$ using the new initial approximation $R_a = R_e$, as shown in Fig. 1(a). We repeat the method, finding the new interception with the horizontal line until $|f(R_a)| < \text{TOL}$. We assume the tolerance (TOL) value is equal to 10^{-10} . In Fig. 1(a), (b), (c), and (d), we show how the method converges to the solution. We see in Fig. 1(d) that the initial approximation is at the exact position of the inflection points, which is precisely at the exact position of $f(R) = 0$. Therefore, our solution is ready.

Figure 3(a), (b), (c), (d), (e), and (f) display the boundaries obtained using the tangent method and varying the γ values from 1 to 6. For each γ , we consider three different ϵ values: $\epsilon_1 = 0.0001$, $\epsilon_2 = 0.5$, and $\epsilon_3 = 0.9999$. In a polygon, the number of edges is directly proportional to the γ value. For $\gamma = 3$, we observe a triangle-like billiard when $\epsilon \rightarrow 1$.

Fig. 3 Sketch of the billiard boundary considering different values of ϵ and γ . The values of ϵ were $\epsilon_1 = 0.0001$, $\epsilon_2 = 0.5$ and $\epsilon_3 = 0.9999$



We recover a square-like billiard for $\gamma = 4$. It is also possible to get a star-like billiard when $\gamma = 5$.

2.3 Method to Obtain the Next Collision with the Billiard Boundary

Our aim now is to explain how to find the position in which a classical particle touches the billiard boundary. To do that, observe Fig. 4(a). Considering a classical particle at the initial angular position θ_0 (measured counterclockwise from the horizontal line), it starts its motion instantly after colliding with the billiard boundary. The particle's initial position (X_0, Y_0) , in Cartesian coordinates, is

$$X_0 = R(\theta_0) \cos(\theta_0) \quad \text{and} \quad Y_0 = R(\theta_0) \sin(\theta_0). \quad (15)$$

We define ϕ_0 as the tangent line's angular direction that passes through the initial position (X_0, Y_0) , leading to

$$\phi_0 = \arctan \left[\frac{Y'(\theta_0)}{X'(\theta_0)} \right] \pmod{2\pi}. \quad (16)$$

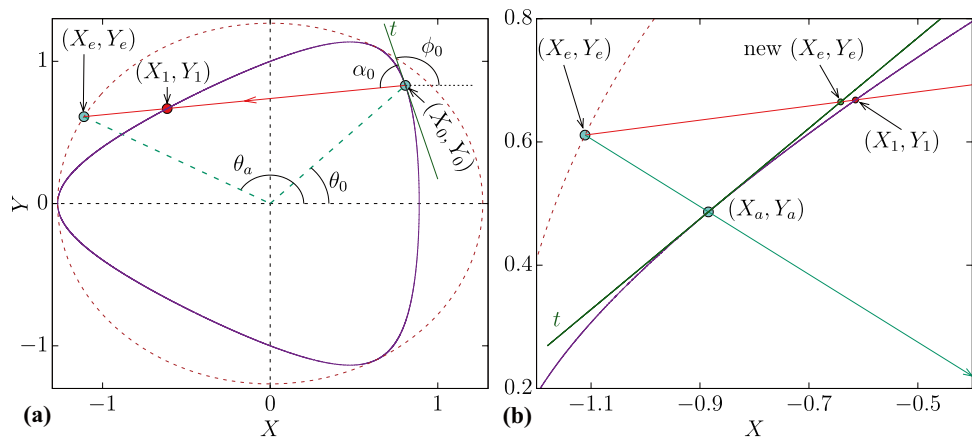
The derivatives X' and Y' are

$$X'(\theta) = \frac{\partial R}{\partial \theta} \cos(\theta) - Y(\theta), \quad (17)$$

and

$$Y'(\theta) = \frac{\partial R}{\partial \theta} \sin(\theta) + X(\theta). \quad (18)$$

Fig. 4 Sketch of the billiard boundary and the angles considered for $\epsilon = 0.6$, $\gamma = 3$, $\theta_0 = 0.8$, and $\alpha_0 = 1.4$



Another critical angle is $\alpha_0 \in (0, \pi)$, which is a complementary angle. With this in mind, we define μ_0 as the angle that gives us the particle's initial direction, written as

$$\mu_0 = \alpha_0 + \phi_0 \pmod{2\pi}. \quad (19)$$

The equations that describe the motion of a classical particle, starting at (X_0, Y_0) , are

$$X_p(\Delta t) = X_0 + V_0 \cos(\mu_0) \Delta t, \quad (20)$$

and

$$Y_p(\Delta t) = Y_0 + V_0 \sin(\mu_0) \Delta t, \quad (21)$$

where (X_p, Y_p) is the particle's position for each time-step Δt .

Now, we consider a circle with radius R_{\max} , which is external to the billiard boundary. The radius of this circle is

$$R_{\max} = R(\pi/\gamma). \quad (22)$$

Figure 4(a) displays an example of trajectory considering the billiard boundary with $\gamma = 3$ and $\epsilon = 0.6$. We set the initial angles as $\theta_0 = 0.8$ and $\alpha_0 = 1.4$. In this figure, we see the outer circle with radius $R_{\max} = R(\pi/3)$.

With all these details in mind, we need to calculate the interception of the particle's trajectory (Eqs. (20) and (21)) and the equation of a circle at the origin, which has a radius $R_{\max}(X^2 + Y^2 = R_{\max}^2)$. It is possible to prove that the interception occurs for the time-step Δt_e given by

$$\Delta t_e = \frac{-b + \sqrt{b^2 - 4 * c}}{2}, \quad (23)$$

where b and c are

$$b = 2[X_0 \cos(\mu_0) + Y_0 \sin(\mu_0)], \quad (24)$$

$$c = X_0^2 + Y_0^2 - R_{\max}^2. \quad (25)$$

The positions of the interception (X_e, Y_e) between the circle and particle's trajectory, in Cartesian coordinates, are

$$X_e = X_0 + \cos(\mu_0) \Delta t_e, \quad (26)$$

$$Y_e = Y_0 + \sin(\mu_0) \Delta t_e. \quad (27)$$

Figure 4(a) shows the interception at (X_e, Y_e) . Our task now is to obtain (X_1, Y_1) . To do that, consider Fig. 4(b). After finding (X_e, Y_e) , we obtain the angular position θ_a of this interception using

$$\theta_a = \arctan\left(\frac{Y_e}{X_e}\right) \pmod{2\pi}. \quad (28)$$

After that, we find the billiard boundary position for the respective angle θ_a , given as $[X_a, Y_a] = [R(\theta_a) \cos(\theta_a), R(\theta_a) \sin(\theta_a)]$ (see Fig. 4(b)).

The tangent line t that passes through (X_a, Y_a) is

$$Y = Y_a + \frac{Y'(\theta_a)}{X'(\theta_a)}(X - X_a). \quad (29)$$

We now calculate the interception of this tangent line and the particle's trajectory (Eqs. (20) and (21)), which happens at the time-step

$$\Delta t_e = \frac{Y_a - Y_0 + \frac{Y'(\theta_a)}{X'(\theta_a)}(X_0 - X_a)}{\sin(\mu_0) - \frac{Y'(\theta_a)}{X'(\theta_a)} \cos(\mu_0)}. \quad (30)$$

The new interception (X_e, Y_e) occurs at $(X_e, Y_e) = (X_0 + \cos(\mu_0) \Delta t_e, Y_0 + \sin(\mu_0) \Delta t_e)$, as shown in Fig. 4(b).

We continue this tangent method, calculating the new θ_a , until $\theta_a - \theta_e < \text{TOL}$ (again set as 10^{-10}). If this condition is confirmed, we consider that this is the angular position of the interception of the particle's trajectory and the billiard boundary, occurring for $\theta_1 = \theta_a$. It is possible to prove, by using trigonometry, that the new angle α_1 is

$$\alpha_1 = \phi_1 - \mu_0 \pmod{\pi}. \quad (31)$$

3 Numerical Results

3.1 Results for $\gamma = 1$

Figure 5 exhibits some numerical results for $\gamma = 1$. We start by considering $\epsilon = 0.4$ in Fig. 5(a), (b), and (c), with the respective phase space shown in Fig. 5(b). Figure 5(a) and (c) display the two orbits and their respective trajectories in blue and red. The blue trajectory is an example of a trajectory that represents an invariant spanning curve. This curve receives this name spanning because it spreads along the entire θ -axis. In contrast, the red curve is an example of an invariant curve (it is not spanning). In the center of these periodic islands, a period-2 elliptical fixed point exists in the position $(\theta, \alpha) = (\pi/2, \pi/2)$ and $(\theta, \alpha) = (3\pi/2, \pi/2)$. There are also hyperbolic fixed points

(unstable fixed points) in the positions $(\theta, \alpha) = (0, \pi/2)$ and $(\theta, \alpha) = (\pi, \pi/2)$. Chaotic behavior emerges close to these hyperbolic fixed points and is named stochastic layers [3].

If we increase the perturbation ϵ to 0.6, we see the chaos, shown in Fig. 5(e), starts to spread along the α -axis. Lots of periodic islands appear and are represented by the blue trajectory in Fig. 5(d). Figure 5(h) displays results when we increase the value of ϵ to 0.8. In blue, we show a trajectory that contains a period-3 elliptical fixed point (Fig. 5(g)), while the red trajectory contains a period-5 fixed point (Fig. 5(i)). Finally, Fig. 5(k) exhibits the phase space for $\epsilon = 0.999$. As one sees, when $\epsilon \rightarrow 1$, the chaos dominates the dynamics. However, a period-2 KAM island remains. In red (Fig. 5(l)), we show an example of the chaotic orbit (trajectory).

3.2 Results for $\gamma = 2$

We consider $\gamma = 2$ and vary the value of ϵ . First, we compute the phase space for $\epsilon = 0.15$, as shown in Fig. 6(b). On the

Fig. 5 Sketch of the billiard boundary for $\gamma = 1$ and different values of ϵ . We consider $\epsilon = 0.4$ in panels (a), (b), and (c); $\epsilon = 0.6$ in panels (d), (e), and (f); $\epsilon = 0.8$ in panels (g), (h), and (i); and finally $\epsilon = 0.999$ in panels (j), (k), and (l)

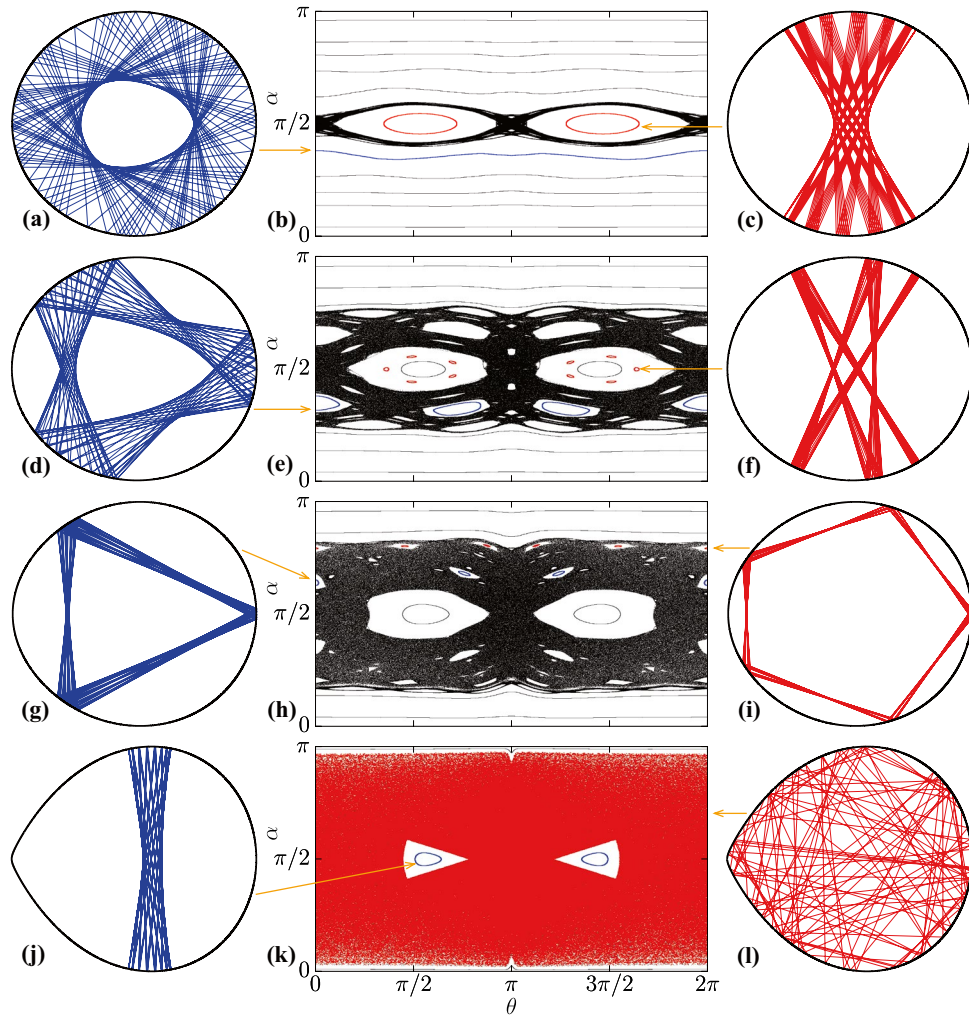
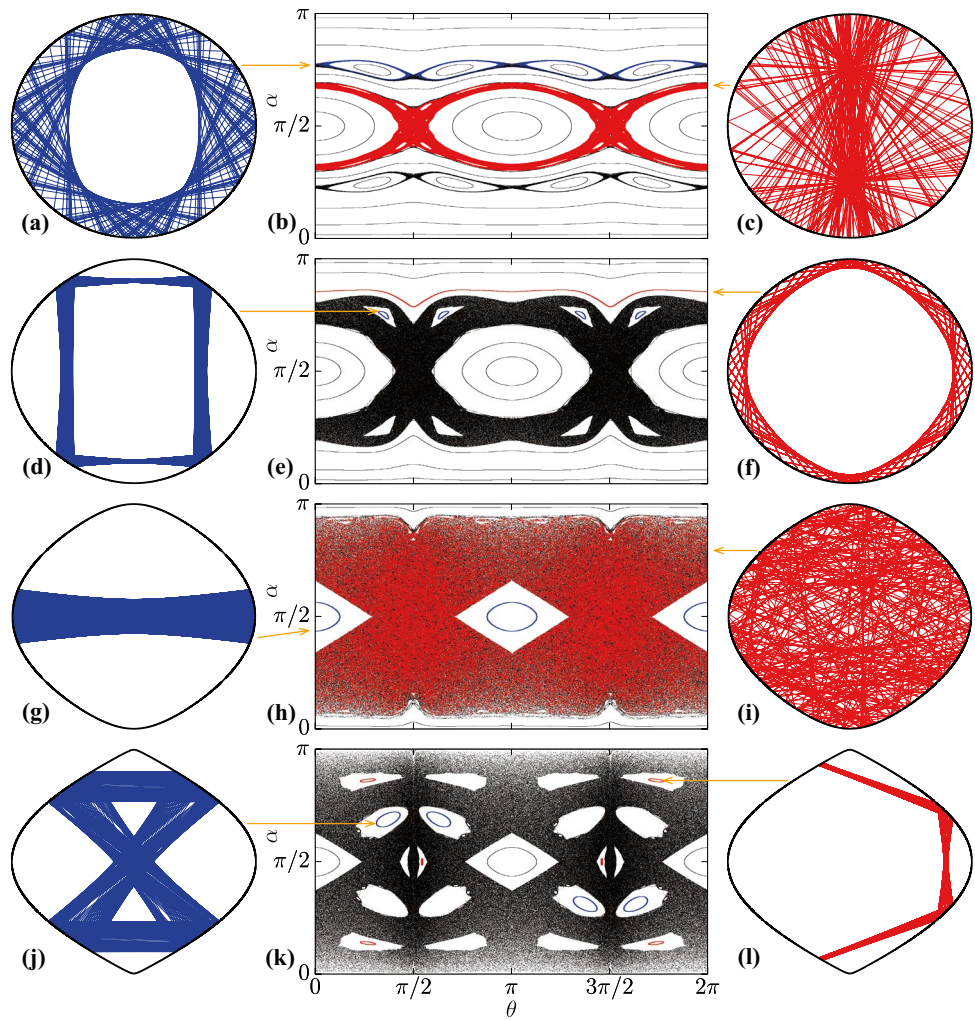


Fig. 6 Sketch of the billiard boundary for $\gamma = 2$ and different values of ϵ . We consider $\epsilon = 0.15$ in panels (a), (b), and (c); $\epsilon = 0.5$ in panels (d), (e), and (f); $\epsilon = 0.9$ in panels (g), (h), and (i); and finally $\epsilon = 0.999$ in panels (j), (k), and (l)



left (Fig. 6(a)), we show a blue trajectory that belongs to a stochastic layer, while on the right (Fig. 6(c)), there is a red stochastic layer. The chaos emerges in three distinct regions (red, blue, and black stochastic layers).

Figure 6(e) exhibits the phase space for a greater value of ϵ , namely $\epsilon = 0.5$. All stochastic layers become a large chaotic region, where all invariant spanning curves between them disappear. We still see some invariant spanning curves, as shown in the red trajectory of Fig. 6(f). The blue invariant curve encloses a period-4 elliptical fixed point in its interior (Fig. 6(d)). If we increase the value of ϵ to 0.9, we see that the chaos multiplies. However, the periodic islands in $(\theta, \alpha) = (0, \pi/2)$ and $(\theta, \alpha) = (\pi, \pi/2)$ remain. On the right, we show an example of a chaotic trajectory (Fig. 6(i)). When $\epsilon \rightarrow 1$ for $\epsilon = 0.999$, some periodic islands appear. On the left, the blue trajectory contains a period-4 fixed point. In contrast, on the right, the red trajectory contains a period-6 elliptical fixed point.

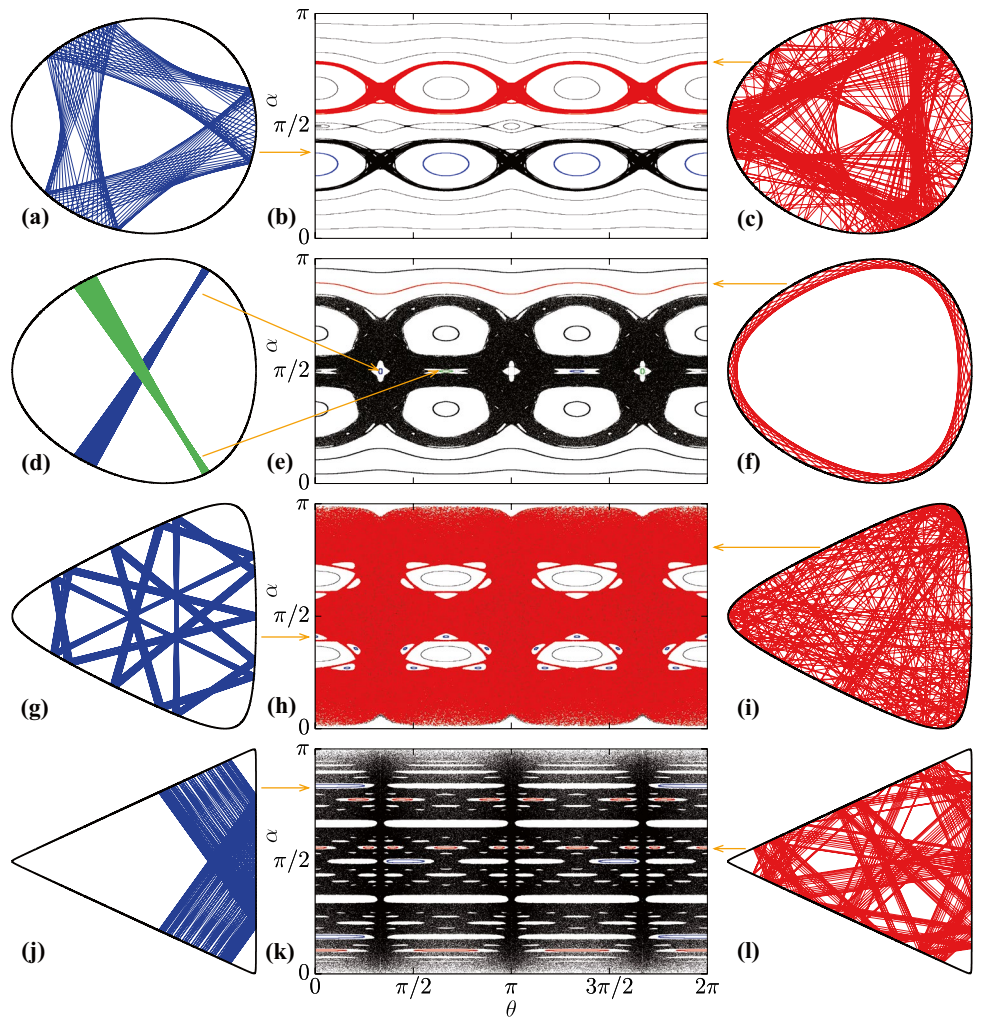
3.3 Results for $\gamma = 3$

In this subsection, we present the results for $\gamma = 3$. Fig. 7(b) displays the phase space with three stochastic layers that exist for $\epsilon = 0.03$. On the right, we show a trajectory that belongs to the red stochastic layer. In contrast, on the left, the blue trajectory encloses a period-3 elliptical fixed point.

When we increase the ϵ value to 0.1 (see Fig. 7(e)), the chaotic regions collapse and create a big chaotic orbit. We verify the existence of two trajectories (blue and green) on the left (item (d)). We observe a red invariant spanning curve on the right of this figure (item (f)).

We identify that the chaos spreads along the α -axis by increasing the ϵ value to 0.8 (Fig. 7(h)). We show a trajectory containing a period-15 elliptical fixed point on the left (item (g)). At the same time, on the right, we see the chaotic orbit (item (i)).

Fig. 7 Sketch of the billiard boundary for $\gamma = 3$ and different values of ϵ . We consider $\epsilon = 0.03$ in panels (a), (b), and (c); $\epsilon = 0.1$ in panels (d), (e), and (f); $\epsilon = 0.8$ in panels (g), (h), and (i); and finally $\epsilon = 0.999$ in panels (j), (k), and (l)



When $\epsilon \rightarrow 1$ ($\epsilon = 0.999$), the phase space shown in Fig. 7(k) presents the appearance of several periodic islands. It happens because the triangular-like billiard is recovered for $\epsilon = 1$. The phase space of a triangular billiard is regular, containing only periodic and quasi-periodic orbits. On the left (item (j)), we show a trajectory that contains a period-4 elliptical fixed point. In contrast, on the right (item (l)), this trajectory contains a period-18 fixed point.

3.4 Maximum Lyapunov Exponent

In this section, we introduce the Lyapunov exponent. It is an essential tool to quantify the average expansion or contraction rate of a small volume of initial conditions. We compute the maximum Lyapunov exponent as a function of ϵ for different γ values, as shown in Fig. 8. [20] define Lyapunov exponent as follows. Let Λ_j (with $j = \{1, 2\}$)

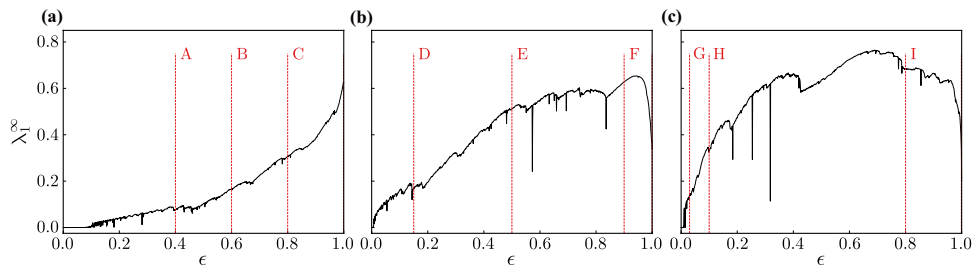


Fig. 8 Maximum Lyapunov exponent as a function of ϵ for (a) $\gamma = 1$, (b) $\gamma = 2$, and (c) $\gamma = 3$ with $\Delta\epsilon = 0.001$. The vertical red dashed lines indicate the values of ϵ shown in Figs. 5, 6, and 7: (A) $\epsilon = 0.4$, (B) $\epsilon = 0.6$, (C) $\epsilon = 0.8$, (D) $\epsilon = 0.15$, (E) $\epsilon = 0.5$, (F) $\epsilon = 0.9$, (G) $\epsilon = 0.03$, (H) $\epsilon = 0.1$, and (I) $\epsilon = 0.8$

be the eigenvalues of $\mathbf{M} = \prod_{i=1}^N \mathbf{J}_i$ and \mathbf{J}_i be the Jacobian matrix evaluated over an orbit that hits the billiard boundary N times. Then,

$$\lambda_j = \lim_{N \rightarrow \infty} \frac{1}{N} \ln \Lambda_j, \quad j = 1, 2, \quad (32)$$

The two values of λ found are symmetric and we can take the highest value (maximum Lyapunov exponent). A positive Lyapunov exponent indicates sensibility to the initial conditions, and as a consequence, the orbit has a chaotic behavior. For $\lambda \rightarrow 0$, the orbit can have periodic or quasi-periodic behaviors. In our simulations, we calculate the Lyapunov exponent for $N = 10^9$ iterations and an orbit initialized inside the largest chaotic component with ϵ varying in an interval according to the step $\Delta\epsilon = 0.001$.

Figure 8(a) displays the maximum Lyapunov exponent for $\gamma = 1$ with an initial condition at $(\theta_0, \alpha_0) = (\pi, \pi/2)$. When the ϵ value increases, on average, the value of λ increases. If we compare the stochastic layer's volume (see Fig. 5) with the maximum Lyapunov exponent for the values of ϵ shown by the red dashed lines, we verify that both increase.

We observe similar results for $\gamma = 2$ and $\gamma = 3$, displayed in Fig. 8(b) and (c), with initial conditions at $(\theta_0, \alpha_0) = (\pi/2, \pi/2)$ and $(\theta_0, \alpha_0) = (\pi, 1.08)$, respectively. In both cases, by varying ϵ , λ grows on average, showing an increase in the stochastic layer's volume. By inspecting the phase spaces in Figs. 6 and 7, for the ϵ values shown by the red dashed lines in Fig. 8, we see that the stochastic layer's volume increases when ϵ increases. The difference between $\gamma = 2, 3$ and $\gamma = 1$ arises when $\epsilon \rightarrow 1$, where there is a decrease in the maximum Lyapunov exponent. Various periodic islands appear, resulting in a reduction of the volume available for the stochastic layer.

Despite the increase, on average, in the maximum Lyapunov exponent with ϵ , there are several ϵ values in which λ falls sharply. We emphasize that the overall behavior of λ does not depend on the initial condition. However, the ϵ values, in which there is a decrease in the maximum Lyapunov exponent, change for different initial conditions. We hypothesize that these falls in λ are due to the stickiness effects [21, 22]. Depending on the initial condition, the orbit can visit a sticky region's neighborhood, causing the observed minimums in λ .

4 Conclusions

We introduce the so-called tunable circular to polygonal billiard. Depending on the control parameter related to the number of edges of our polygon (γ), we can recover several polygons. It is a generalization of a triangular-like billiard shown by Arita and collaborators in Ref. [1]. We show, in

detail, how to find the radius of the billiard boundary, where we apply a tangent method to speed up the numerical findings. After that, we detail how to obtain the interception of the particle's trajectory and billiard boundary. We again use a tangent method to solve this transcendental equation.

We present the phase space and some examples of trajectories for γ equal to 1, 2, and 3. In the last part of the paper, we display the corresponding Lyapunov exponent for several deformations ϵ . Their values depend on the size of the chaotic sea given by the boundaries. Also, we show that the Lyapunov exponent abruptly falls for specific parameter values due to stickiness.

Acknowledgements DRC acknowledges São Paulo Research Foundation (FAPESP, Brazil) (Grant No. 2020/02415-7) and National Council for Scientific and Technological Development (CNPq, Brazil) (Grant No. 162944/2020-9). The authors also acknowledge Coordenação de Aperfeiçoamento de Pessoal de Nível Superior (CAPES) and Fundação Araucária.

Declarations

Conflict of Interest The authors declare no competing interests.

References

1. K.I. Arita, M. Brack, Anomalous shell effect in the transition from a circular to a triangular billiard. *Phys. Rev. E* **77**(5) 056211 (2008)
2. M.V. Berry, Regularity and chaos in classical mechanics, illustrated by three deformations of a circular 'billiard'. *Eur. J. Phys.* **2**(2), 91–102 (1981). <https://doi.org/10.1088/0143-0807/2/2/006>
3. E.D. Leonel, L. Bunimovich, Suppressing Fermi acceleration in a driven elliptical billiard. *Phys. Rev. Lett.* **104**, 224101 (2010). <https://doi.org/10.1103/PhysRevLett.104.224101>
4. J.P. Bird, Recent experimental studies of electron transport in open quantum dots. *J. Phys. Condens. Matter.* **11**(38), R413–R437 (1999). <https://doi.org/10.1088/0953-8984/11/38/201>
5. V. Milner, J.L. Hanssen, W.C. Campbell, M.G. Raizen, Optical billiards for atoms. *Phys. Rev. Lett.* **86**, 1514–1517 (2001). <https://doi.org/10.1103/PhysRevLett.86.1514>
6. N. Friedman, A. Kaplan, D. Carasso, N. Davidson, Observation of chaotic and regular dynamics in atom-optics billiards. *Phys. Rev. Lett.* **86**, 1518–1521 (2001). <https://doi.org/10.1103/PhysRevLett.86.1518>
7. M.F. Andersen, T. Grünzweig, A. Kaplan, N. Davidson, Revivals of coherence in chaotic atom-optics billiards. *Phys. Rev. A* **69**, 063413 (2004). <https://doi.org/10.1103/PhysRevA.69.063413>
8. M.F. Andersen, A. Kaplan, T. Grünzweig, N. Davidson, Decay of quantum correlations in atom optics billiards with chaotic and mixed dynamics. *Phys. Rev. Lett.* **97**, 104102 (2006). <https://doi.org/10.1103/PhysRevLett.97.104102>
9. H.D. Gräf, H.L. Harney, H. Lengeler, C.H. Lewenkopf, C. Rangacharyulu, A. Richter, P. Schardt, H.A. Weidenmüller, Distribution of eigenmodes in a superconducting stadium billiard with chaotic dynamics. *Phys. Rev. Lett.* **69**, 1296–1299 (1992). <https://doi.org/10.1103/PhysRevLett.69.1296>

10. T. Sakamoto, Y. Takagaki, S. Takaoka, K. Gamo, K. Murase, S. Namba, Electron focusing in a widely tapered cross junction. *Jpn. J. Appl. Phys.* **30**(Part 2, No. 7A), L1186–L1188 (1991). <https://doi.org/10.1143/jjap.30.11186>
11. D. Sweet, B.W. Zeff, E. Ott, D.P. Lathrop, Three-dimensional optical billiard chaotic scattering. *Physica D: Nonlinear Phenomena* **154**(3), 207–218 (2001). [https://doi.org/10.1016/S0167-2789\(01\)00235-4](https://doi.org/10.1016/S0167-2789(01)00235-4)
12. D.R. da Costa, M.R. Silva, E.D. Leonel, Escape beam statistics and dynamical properties for a periodically corrugated waveguide. *Commun. Nonlinear Sci. Numer. Simul.* **19**(4), 842–850 (2014). <https://doi.org/10.1016/j.cnsns.2013.08.009>
13. M.R. Silva, D.R. da Costa, E.D. Leonel, Characterization of multiple reflections and phase space properties for a periodically corrugated waveguide. *J. Phys. A Math. Theor.* **45**(26), 265101 (2012). <https://doi.org/10.1088/1751-8113/45/26/265101>
14. E.D. Leonel, D.R. da Costa, C.P. Dettmann, Scaling invariance for the escape of particles from a periodically corrugated waveguide. *Phys. Lett. A* **376**(4), 421–425 (2012). <https://doi.org/10.1016/j.physleta.2011.11.027>
15. E. Persson, I. Rotter, H.J. Stöckmann, M. Barth, Observation of resonance trapping in an open microwave cavity. *Phys. Rev. Lett.* **85**, 2478–2481 (2000). <https://doi.org/10.1103/PhysRevLett.85.2478>
16. E.D. Leonel, Corrugated waveguide under scaling investigation. *Phys. Rev. Lett.* **98**, 114102 (2007). <https://doi.org/10.1103/PhysRevLett.98.114102>
17. C.M. Marcus, A.J. Rimberg, R.M. Westervelt, P.F. Hopkins, A.C. Gossard, Conductance fluctuations and chaotic scattering in ballistic microstructures. *Phys. Rev. Lett.* **69**, 506–509 (1992). <https://doi.org/10.1103/PhysRevLett.69.506>
18. J. Stein, H.J. Stöckmann, Experimental determination of billiard wave functions. *Phys. Rev. Lett.* **68**, 2867–2870 (1992). <https://doi.org/10.1103/PhysRevLett.68.2867>
19. G. Del Magno, J. Lopes Dias, P. Duarte, J. Pedro Gaivão, D. Pinheiro, Chaos in the square billiard with a modified reflection law. *Chaos: An Interdisciplinary Journal of Nonlinear Science* **22**(2), 026106 (2012)
20. J.P. Eckmann, D. Ruelle, Ergodic theory of chaos and strange attractors. *Rev. Mod. Phys.* **57**, 617–656 (1985). <https://doi.org/10.1103/RevModPhys.57.617>
21. E.G. Altmann, A.E. Motter, H. Kantz, Stickiness in Hamiltonian systems: from sharply divided to hierarchical phase space. *Phys. Rev. E* **73**, 026207 (2006). <https://doi.org/10.1103/PhysRevE.73.026207>
22. M.S. Santos, M. Mugnaine, J.D. Szezech, A.M. Batista, I.L. Caldas, R.L. Viana, Using rotation number to detect sticky orbits in Hamiltonian systems. *Chaos: An Interdisciplinary Journal of Nonlinear Science* **29**(4), 043125 (2019). <https://doi.org/10.1063/1.5078533>

Publisher's Note Springer Nature remains neutral with regard to jurisdictional claims in published maps and institutional affiliations.